Atomistic simulation and XAS investigation of Mn induced defects in $Bi_{12}TiO_{20}$

Marcos V dos S. Rezende[1], Denise J Santos[2], Robert A Jackson[3], Mário E G Valerio[2], Zélia S Macedo[2]

[1]Functional Nanomaterials Group, Physics Department, Federal University of Sergipe, Campus Universitário Professor Alberto Carvalho, 49500-000 Itabaiana-SE, Brazil

[2]Physics Department, Federal University of Sergipe, São Cristovão, 49000-000, SE, Brazil

[3]School of Physical and Geographical Sciences, Keele University, Keele, Staffordshire ST5 5BG, UK

Abstract – This work reports an investigation of the valence and site occupancy of Mn dopants in $Bi_{12}TiO_{20}$ (BTO: Mn) host using X-ray Absorption (XAS) and atomistic simulation techniques based on energy minimisation. X-ray Absorption Near Edge Structure (XANES) at the Mn K-edges gave typical results for Mn ions with mixed valences of 3+ and 4+. Extended X-ray Absorption Fine Structure (EXAFS) results indicated that Mn ions are probably substituted at Ti sites. Atomistic simulation was performed assuming the incorporation of Mn^{2+}, Mn^{3+} and Mn^{4+} ions at either Bi^{3+} or Ti^{4+} sites, and the results were compared to XANES and EXAFS measurements. Electrical conductivity for pure and doped samples was used to evaluate the consistency of the proposed model.

Keywords : Doped bismuth titanate, charge transport mechanism, sillenite.

1. Introduction

Sillenite-type crystals with chemical composition $Bi_{12}MO_{20}$ (M= Si, Ge, Ti) belong to the cubic space group I23 and exhibit piezoelectric, electro-optical, elasto-optical, and photoconductive properties [1–6]. The combination of electro-optical and photoconductivity properties results in the so-called photorefractive effect[7,8]. Due to these properties, sillenite crystals are useful for many advanced and promising applications, such as a reversible recording medium for real-time holography, image processing applications, coherent light amplification, optical phase conjugation, optical information processing, optical interconnection and communications [7,9]. Their photoconductivity is believed to be of *n*-type whereas their dark conductivity is of *p*-type [10].

Bismuth titanium oxide crystals, $Bi_{12}TiO_{20}$ (BTO), have some practical advantages compared to their isomorphs $Bi_{12}SiO_{20}$ (BSO) and $Bi_{12}GeO_{20}$ (BGO), including lower optical activity, larger electro-optic and photoconductivity coefficients and higher

sensitivity to red light [7]. As with most photorefractive materials, BTO presents a rich defect structure, the nature of which is still a matter of active research. Doping sillenites with different elements has been tried in the hope of improving their characteristics and also to provide better understanding of the mechanisms and active centres involved in the recording process [11]. Point defects, either intrinsic or extrinsic, play a fundamental role in the BTO properties. Defect identification, including the dopant ions involved, their valence state and site occupation is essential since this information may guide the efforts for optimisation of the synthesis conditions to obtain the intended properties. The BTO structure is given in figure 1.

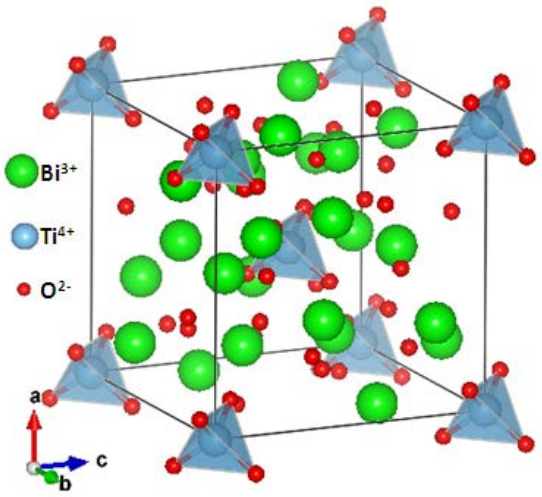

Figure 1 – The structure of BTO

Bi/M antisite defects, consisting of a Bi^{3+} ion in a tetrahedral M^{4+} site, were suggested as the most probable intrinsic defect in sillenites, with charge compensation by a hole associated with the Bi^{3+} ion. Doping with transition metals is known to have a significant effect on the spectroscopic properties of BTO [12,13]. It was previously reported that Mn substitutes for M^{4+} cations in $Bi_{12}MO_{20}$ structure, with an oxidation state varying from 5+ to 2+ [14]. Different oxidation states and/or occupation sites would result in different effects on the spectroscopic properties causing different absorption/emission spectra, and may influence the density of charge carriers, so it is very important to study the BTO structure containing Mn-dopants.

X-ray absorption spectroscopy (XAS) is a powerful tool for determining the local structural information of compounds. The XAS spectrum has two typical regions, named as near-edge (XANES) and extended fine structure (EXAFS). The first region provides local chemical information, while the latter is used to obtain information about the local arrangement of elements surrounding absorbing atom [15]. In a previous work [16] atomistic simulation was used to study the intrinsic defect, ion migration and rare earth ion incorporation in the $Bi_{12}TiO_{20}$ host. It was shown that Schottky defects, which are formed by only vacancy species, are most likely followed by oxygen Frenkel defects, which are formed by vacancy and interstitial pairs. The incorporation of the rare earth ions was found to be more favourable at the Bi^{3+} site, but becomes less favourable going along the lanthanide group. Atomistic simulation

was also used to study intrinsic and extrinsic defects in other titanates, for example, $Bi_4Ti_3O_{12}$ [17], $Bi_{12}GeO_{20}$ and $Bi_4Ge_3O_{12}$ [18].

In this work, X-ray Absorption Near Edge Structure (XANES) and Extended X-ray Absorption Fine Structure (EXAFS) were used to investigate, respectively, valence state and occupied site symmetry in manganese-doped BTO. Atomistic simulation was also used to help the interpretation of XANES/EXAFS and of the conductivity data.

2. Method

2.1. Experimental

Pure and doped $Bi_{12}TiO_{20}$ samples were obtained by solid-state reaction. The precursors used in stoichiometric proportions were the oxides Bi_2O_3 (Alfa Aesar, 99.99%), TiO_2 (Merck, 99.9%) and 0.5 mol% $Mn(NO_3)_2$+$4H_2O$ (Merck, 98.5%). These precursors were ground in agate mortar and calcined at 700°C for 6 hours in an alumina crucible in an open atmosphere furnace.

The structural investigation and phase formation were carried out by powder X-ray diffraction technique in a XRD–Rigaku RINT 2000/PC, using Cu Kα radiation. The measurements were performed at room temperature in step-scan mode, in the 2θ range between 10° and 80°, with steps of 0.02° and acquisition time of 10 s. The diffraction patterns were analysed according to the Rietveld profile refinement method using DBWS software[19]. The valence of the dopant and their site symmetry in the BTO matrix were investigated by XANES and EXAFS, measured at the D08B:XAFS2 beamline of the Brazilian Synchrotron Light Laboratory (LNLS, proposal XAFS1#9349) in Campinas/SP, Brazil. XANES and EXAFS spectra were acquired in fluorescence mode using incident photon energies around the Mn K-edge (6539 eV). Mn metallic foils were used to calibrate the beamline monochromator. Reference materials MnO, Mn_2O_3 and MnO_2 were also measured and used to check the valence of the Mn ions in the sample.

For AC conductivity measurements, the powder samples were pressed into the form of discs and sintered at 800 ^oC for 2h [20]. Electric contact was made by applying Pt paste on the parallel faces of the samples and firing them at 700 °C for 30 min. The measurements were carried out isothermally, in a Solartron 1260 Impedance Analyser, at frequency of 10 kHz.

2.2. Simulation

The calculations employed in this work are based on an atomistic model and energy minimisation. Energy minimisation is a method which allows the atomic coordinates to iteratively converge towards the atomic configuration with minimum total energy. In this method, the atomic positions are described in terms of classical potential models. The potential is used to express the interaction between the atoms. It takes into account the long-range Coulomb potential and both repulsive and attractive short-range contributions via the Buckingham potential. The electronic

polarization effects are included by the core-shell model as described by Dick and Overhauser [21]. This model treats such effects in terms of a shell with charge *Y* connected to a core with charge *Z–Y,* where *Z* is the formal charge of the ion by an isotropic harmonic spring of force constant *k*. The shell nominally represents the valence electron cloud, and the core represents the nucleus plus core electrons. All calculations were made with the GULP code [22]. A set of pair-potential parameters was derived for the $Bi_{12}TiO_{20}$ host in the previous work [16] wherein the Bi-O, Ti-O and O-O parameters were refitted using an initial parameterisation already used for $BaTiO_3$ [23] and BGO [18]. The observed difference between experimental and simulated structure are less than 0.1%. The Mn-O parameters used in MnO, Mn_2O_3 and MnO_2 were fitted using an initial parameterisation obtained by Lewis and Catlow [24].

The defect energies were calculated by the Mott−Littleton method [25]. This method consists of the division of crystal lattice surrounding a defect into two spherical regions. The first region is immediately surrounding the defects (region I), where interactions between atoms are treated explicitly and the ions are allowed to fully relax. The second region, comprising more distant ions, is treated as a dielectric continuum. Consistent region sizes of 16 and 18 Å for regions I and IIA were used in the calculations, following tests to ensure convergence had been reached. This methodology implicitly assumes that each defect is isolated in an infinite matrix and so it has to be viewed as a good approximation for diluted systems, where the concentration of dopants are low enough to consider each defect generated by them homogenously distributed in the solid matrix.

3. Results and discussion

Figure 2 presents the Rietveld refinement of the XRD (X-ray Diffraction) pattern of $Bi_{12}TiO_{20}$ doped with 0.5 mol% Mn (called BTO: Mn hereafter) crystallised at 700 °C for 6 hours. The refinement employed a pseudo-Voigt function and used the Swindells [26] crystallographic data as starting parameters. The dots represent the experimental points and the solid line the refined pattern. The bottom part of the figure displays the difference between the measured and calculated data, indicating that a quite good structural refinement was achieved. The result confirms a cubic structure and space group I23 at room temperature. No other crystalline phase was detected. Table 1 presents the cell parameters and atomic positions, as well as the quality parameters for the refinement. The R_p, R_{wp} and R_{Bragg} values are low, confirming the quality of the results. The cell parameters a = b = c = 10.1627 ± 0.0001 Å are comparable to the values a = b = c = 10.1722 ± 0.0001 Å previously reported for pure samples [20].

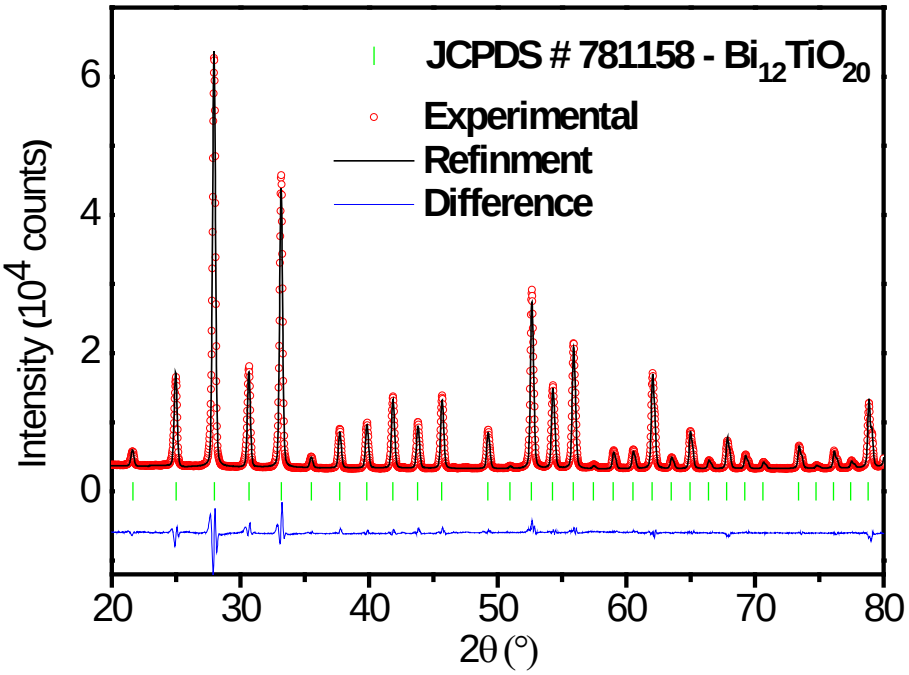

Figure 2 – Refined XRD pattern of BTO: Mn.

Table 1 – Summary of the main parameters from the Rietveld refinement of cubic BTO: Mn.

a (Å)	10.1627	**R_p**	7.64%
V (Å^3)	1049.599	**R_{wp}**	10.85%
ρ (g/cm^3)	9.102	**R_{Bragg}**	3.44
Fractional coordinates	**x**	**y**	**z**
Bi	0.1766	0.3177	0.0161
Ti	0.0000	0.0000	0.0000
O1	0.1270	0.2491	0.4988
O2	0.1960	0.1960	0.1960
O3	-0.1509	-0.1509	-0.1509

R_p = pattern R-factor; R_{wp} = weighted pattern R-factor, R_B = Bragg R-factor

An in depth understanding of the incorporation of Mn in the BTO matrix can be obtained from atomistic simulation considering the three possible oxidation states of Mn. In this work, incorporation of Mn^{2+}, Mn^{3+} and Mn^{4+} ions at the Bi^{3+} site or at the Ti^{4+} site were simulated. In some cases, it was necessary to include charge compensating defects such as an oxygen vacancy, an interstitial bismuth ion, an interstitial titanium ion, or a trapped hole. Firstly, we consider the incorporation of Mn^{2+} ion at Bi^{3+} sites. A possible from of charge compensation could occur by oxygen vacancy formation. Eq. (1a) presents this defect reaction:

$$2MnO + 2Bi_{Bi} \rightarrow (2Mn'_{Bi} + V_O^{\bullet\bullet}) + Bi_2O_3 \qquad (1a)$$

The solution energy (E_{sol}) associated with this defect is calculated according to Eq. (1b). It takes into account lattice energies (E_{latt}) and formation energies of each defect (E_{def}).

$$E_{Sol} = 2E_{def}\left[Mn'_{Bi}\right] + E_{def}\left[V_O^{\bullet\bullet}\right] + E_{latt}\left[Bi_2O_3\right] - 2E_{latt}\left[MnO\right] \quad (1b)$$

The other possible charge compensation mechanisms are interstitial bismuth (Equations 2a and 2b), interstitial titanium (Equations 3a and 3b), or a trapped hole next to Mn^{2+} in Bi^{3+} site (Equations 4a and 4b):

$$3MnO + 3Bi_{Bi} \rightarrow (3Mn'_{Bi} + Bi_i^{\bullet\bullet\bullet}) + Bi_2O_3 \quad (2a)$$

$$E_{Sol} = 3E_{def}\left[Mn'_{Bi}\right] + E_{def}\left[Bi_i^{\bullet\bullet\bullet}\right] + E_{latt}\left[Bi_2O_3\right] - 3E_{latt}\left[MnO\right] \quad (2b)$$

$$4MnO + 4Bi_{Bi} + TiO_2 \rightarrow (4Mn'_{Bi} + Ti_i^{\bullet\bullet\bullet\bullet}) + 2Bi_2O_3 \quad (3a)$$

$$E_{Sol} = 4E_{def}\left[Mn'_{Bi}\right] + E_{def}\left[Ti_i^{\bullet\bullet\bullet\bullet}\right] + 2E_{latt}\left[Bi_2O_3\right] - 3E_{latt}\left[MnO\right] - E_{latt}\left[TiO_2\right] \quad (3b)$$

$$MnO + Bi_{Bi} + 0.25O_2(g) \rightarrow (Mn'_{Bi} + h^{\bullet}) + 0.5Bi_2O_3 \quad (4a)$$

$$E_{Sol} = E_{def}\left[Mn'_{Bi}\right] + E_{def}\left[h^{\bullet}\right] + 0.5E_{latt}\left[Bi_2O_3\right] + 0.25D(O_2) + 0.5E_A^{O^{2-}} - E_{latt}\left[MnO\right] \quad (4b)$$

Another possible scenario involves Mn^{2+} at a Ti^{4+} site with charge compensation by oxygen vacancies (Equations 5a and 5b), interstitial bismuth (Equations 6a and 6b), interstitial titanium (Equations 7a and 7b), or a trapped hole (Equations 8a and 8b):

$$MnO + Ti_{Ti} \rightarrow (Mn''_{Ti} + V_O^{\bullet\bullet}) + TiO_2 \quad (5a)$$

$$E_{Sol} = E_{def}\left[Mn''_{Ti}\right] + E_{def}\left[V_O^{\bullet\bullet}\right] + E_{latt}\left[TiO_2\right] - E_{latt}\left[MnO\right] \quad (5b)$$

$$3MnO + 3Ti_{Ti} + Bi_2O_3 \rightarrow (3Mn''_{Ti} + 2Bi_i^{\bullet\bullet\bullet}) + 3TiO_2 \quad (6a)$$

$$E_{Sol} = 3E_{def}\left[Mn''_{Ti}\right] + 2E_{def}\left[Bi_i^{\bullet\bullet\bullet}\right] + E_{latt}\left[TiO_2\right] - 3E_{latt}\left[MnO\right] - E_{latt}\left[Bi_2O_3\right] \quad (6b)$$

$$2MnO + 2Ti_{Ti} \rightarrow (2Mn''_{Ti} + Ti_i^{\bullet\bullet\bullet\bullet}) + TiO_2 \quad (7a)$$

$$E_{Sol} = 2E_{def}\left[Mn''_{Ti}\right] + E_{def}\left[Ti_i^{\bullet\bullet\bullet\bullet}\right] + E_{latt}\left[TiO_2\right] - 2E_{latt}\left[MnO\right] \quad (7b)$$

$$MnO + Ti_{Ti} + 0.5O_2(g) \rightarrow (Mn''_{Ti} + 2h^{\bullet}) + TiO_2 \quad (8a)$$

$$E_{Sol} = E_{def}\left[Mn''_{Ti}\right] + 2E_{def}\left[h^{\bullet}\right] + 0.5E_{latt}\left[TiO_2\right] + 0.5D(O_2) + E_A^{O^{2-}} - E_{latt}\left[MnO\right] \quad (8b)$$

Next Mn with valence 3+ substituting either at Bi^{3+} or Ti^{4+} sites is considered. For substitution at Bi^{3+} sites, no charge-compensating defect is required and the defect reaction and energy are presented in Eqs (9a) and (9b) respectively. On the other hand, substitution at the Ti^{4+} site would require charge compensation by oxygen vacancies, interstitial bismuth, interstitial titanium, or trapped holes. The respective reactions and energies associated to these defects are presented in Equations 10-13.

$$0.5Mn_2O_3 + Bi_{Bi} \rightarrow Mn_{Bi}^{\times} + 0.5Bi_2O_3 \quad (9a)$$

$$E_{Sol} = E_{def}\left[Mn_{Bi}^{\times}\right] + 0.5E_{latt}\left[Bi_2O_3\right] - 0.5E_{latt}\left[Mn_2O_3\right] \quad (9b)$$

$$Mn_2O_3 + 2Ti_{Ti} \rightarrow (2Mn'_{Ti} + V_O^{\bullet\bullet}) + 2TiO_2 \quad (10a)$$

$$E_{Sol} = 2E_{def}\left[Mn'_{Ti}\right] + E_{def}\left[V_O^{\bullet\bullet}\right] + 2E_{latt}\left[TiO_2\right] - E_{latt}\left[Mn_2O_3\right] \quad (10b)$$

$$1.5Mn_2O_3 + 2Ti_{Ti} + 0.5Bi_2O_3 \rightarrow (3Mn'_{Ti} + Bi_i^{\bullet\bullet\bullet}) + 3TiO_2 \quad (11a)$$

$$E_{Sol} = 3E_{def}\left[Mn'_{Ti}\right] + E_{def}\left[Bi_i^{\bullet\bullet\bullet}\right] + 3E_{latt}\left[TiO_2\right] - 1.5E_{latt}\left[Mn_2O_3\right] - 0.5E_{latt}\left[Bi_2O_3\right] \quad (11b)$$

$$2Mn_2O_3 + 4Ti_{Ti} \rightarrow (4Mn'_{Ti} + Ti_i^{\bullet\bullet\bullet\bullet}) + 4TiO_2 \quad (12a)$$

$$E_{Sol} = 3E_{def}\left[Mn'_{Ti}\right] + E_{def}\left[Bi_i^{\bullet\bullet\bullet}\right] + 3E_{latt}\left[TiO_2\right] - 1.5E_{latt}\left[Mn_2O_3\right] - 0.5E_{latt}\left[Bi_2O_3\right] \quad (12b)$$

$$0.5Mn_2O_3 + Ti_{Ti} + 0.25O_2(g) \rightarrow (Mn'_{Ti} + h^{\bullet}) + TiO_2 \quad (13a)$$

$$E_{Sol} = E_{def}\left[Mn'_{Ti}\right] + E_{def}\left[h^{\bullet}\right] + E_{latt}\left[TiO_2\right] + 0.25D(O_2) + 0.5E_A^{O^{2-}} - 0.5E_{latt}\left[Mn_2O_3\right] \quad (13b)$$

Finally, Mn can assume valence 4+ when it is incorporated at either Bi^{3+} or Ti^{4+} sites. For substitutional defects at Ti^{4+} sites, no charge-compensation is required. However, for the incorporation at the Bi^{3+} site, the charge neutrality can be achieved by interstitial oxygen, bismuth vacancy, titanium vacancy or a trapped electron near the substitutional Mn^{4+}. The reactions and energies describing each of these possible conditions are presented below (Equations 14-18).

$$2MnO_2 + 2Bi_{Bi} \rightarrow (2Mn_{Bi}^{\bullet} + O_i'') + Bi_2O_3 \quad (14a)$$

$$E_{Sol} = 2E_{def}\left[Mn_{Bi}^{\bullet}\right] + E_{def}\left[O_i''\right] + E_{latt}\left[Bi_2O_3\right] - 2E_{latt}\left[MnO_2\right] \quad (14b)$$

$$3MnO_2 + 4Bi_{Bi} \rightarrow (3Mn_{Bi}^{\bullet} + V_{Bi}''') + 2Bi_2O_3 \quad (15a)$$

$$E_{Sol} = 3E_{def}\left[Mn_{Bi}^{\bullet}\right] + E_{def}\left[V_{Bi}'''\right] + 2E_{latt}\left[Bi_2O_3\right] - 3E_{latt}\left[MnO_2\right] \quad (15b)$$

$$4MnO_2 + 4Bi_{Bi} \rightarrow (4Mn_{Bi}^{\bullet} + V_{Ti}'''') + 2Bi_2O_3 + TiO_2 \quad (16a)$$

$$E_{Sol} = 4E_{def}\left[Mn_{Bi}^{\bullet}\right] + E_{def}\left[V_{Ti}''''\right] + 2E_{latt}\left[Bi_2O_3\right] + E_{latt}\left[TiO_2\right] - 4E_{latt}\left[MnO_2\right] \quad (16b)$$

$$MnO_2 + Bi_{Bi} \rightarrow (Mn_{Bi}^{\bullet} + e') + 0.5Bi_2O_3 + 0.25O_2(g) \quad (17a)$$

$$E_{Sol} = E_{def}\left[Mn'_{Ti}\right] + E_{def}\left[e'\right] + 0.5E_{latt}\left[Bi_2O_3\right] - 0.25D(O_2) - 0.5E_A^{O^{2-}} - E_{latt}\left[MnO_2\right] \quad (17b)$$

$$MnO_2 + Ti_{Ti} \rightarrow Mn_{Ti}^{\times} + TiO_2 \quad (18a)$$

$$E_{Sol} = E_{def}\left[Mn_{Ti}^{\times}\right] + E_{latt}\left[TiO_2\right] - E_{latt}\left[MnO_2\right] \quad (18b)$$

In order to evaluate the most likely defect for each valence of Mn, the solution energies E_{sol} were calculated for each case and are presented in Tables 3, 4 and 5. The model used for the hole state is the same as the O^- ion, while electron states are represented by Ti^{2+} and Ti^{3+} species. Electron and hole formation energies are calculated by combining GULP interatomic energies with free-ion intra-atomic energies, i.e., the second electron affinity of oxygen [27], the fourth adjusted potential of titanium, and the third ionization potential of bismuth [28]. Here the simplifying assumption is made that such ionization energies differ little from the free atom values. These values are also given in Table 5.

Table 3 –Lattice energies calculated for $Bi_{12}TiO_{20}$ and the starting oxides (eV)

Compound	$E_{Lattice}$
$Bi_{12}TiO_{20}$	-888.03
Bi_2O_3	-127.03
TiO_2	-111.09
MnO	-38.26
Mn_2O_3	-148.26
MnO_2	-120.99

Table 4 – Calculated energy for electron-hole formation in $Bi_{12}TiO_{20}$ (eV).

Calculated terms(E_S)	$Bi_{12}TiO_{20}$
$Bi_{Bi}=(e')$	24.25
$Ti_{Ti}=(e')$	40.73
$O_O=(h)$	11.67
$Bi^{2+}\rightarrow e'+Bi^{3+}$[36]	25.56
$Ti^{3+}\rightarrow e'+Ti^{4+}$[36]	43.27
$O^{-}+e'\rightarrow O^{2-}$[35]	8.199
$e= E_S^{Bi}+E_e$	-1.31
$e= E_S^{Ti}+E_e$	-2.54
$h=E_S^{O}+E_h$	3.47

Table 5 – Formation energy calculated for basic defects in $Bi_{12}TiO_{20}$ host (Interstitial position at (1/2, 0, 0))

Defect	Formation energy(eV)	Defect	Formation energy(eV)
V_{Bi}'''	48.90	$Mn_{Bi}'(Mn^{2+})$	21.13
V_{Ti}''''	93.80	$Mn_{Bi}(Mn^{3+})$	-7.51
$V_{O1}^{\bullet\bullet}$	17.00	$Mn_{Bi}^{\bullet}(Mn^{4+})$	-47.57
$V_{O2}^{\bullet\bullet}$	17.00	$Mn_{Ti}''(Mn^{2+})$	60.60
$V_{O3}^{\bullet\bullet}$	16.70	$Mn_{Ti}'(Mn^{3+})$	29.64
$Bi_{i1}^{\bullet\bullet\bullet}$	-24.80*	$Mn_{Ti}(Mn^{4+})$	-11,48
$Ti_{i1}^{\bullet\bullet\bullet\bullet}$	-68.50*		
O_{i1}''	-8.90*		

The energy required to create a trapped hole is given by summing the energy required (in the gas phase) for the process $O^{2-}\rightarrow O^{1-}+e^{-}$, plus the substitutional defect energy required to replace an O^{-} ion on a regular O^{2-} site. This model was used to describe a trapped hole in an O^{2-} ion nearby the Bi-Ti antisite. The energy required to create an electron is given by summing the energy required (in the gas phase) for the process $Ti^{4+}+ e^{-} \rightarrow Ti^{3+}$, plus the substitutional defect energy required to replace an Ti^{3+} ion on a regular Ti^{4+} site. Alternatively, it can be given by summing the energy required (in the gas phase) for the process $Bi^{3+}+ e^{-} \rightarrow Bi^{2+}$ and the substitutional defect energy required to replace an Bi^{2+} ion on a regular Bi^{3+}. The meaning of these two last processes is that the electron can be captured either by the Bi^{3+} or the Ti^{4+} that is close to the dopant site.

The energies of all reactions can then be calculated by combining the appropriate defect and lattice energy terms (Bi_2O_3, TiO_2, MnO, Mn_2O_3 and MnO_2 oxides), as showed in equations 1 to 18. This consistent approach provides a guide to the relative energies for different dopant ions on different lattice sites. The solution energy was normalized by the number of the dopants presented in each defect.

The solution energies per dopant ion obtained from these calculations are shown in Table 6. For the incorporation of the Mn^{2+} ion, it can be seen, from the solution energies, that schemes involving the substitution of Mn^{2+} ion at the Bi^{3+} site compensated by a hole captured by an O^{2-} ion is the most favourable defect. All defect incorporation schemes can be ranked, from lowest to highest energies, and the ones that should be also considered are the two lowest ones, that showed solution energies close to the ($Mn_{Bi}' + h^{\bullet}$). The solution energy of the incorporation of Mn^{2+} at the Ti^{4+} sites also compensated by hole defects, ($Mn_{Ti}'' + 2h^{\bullet}$) was calculated to be 3% higher than the previous one. This relatively small solution energy differences suggest the possibility of a Mn^{2+} ion substituting at both cationic host sites. This can be explained in terms of the size difference between the Mn^{2+} ion and the host matrix cations (ΔR) given in Table 7. The values are based on the modulus of the difference of the ionic radii of Bi^{3+} and Ti^{4+} ($R_h(CN)$) and the ionic radii of the doped ion ($R_d(CN)$), where CN is the coordination number. Ionic radii were taken from Shannon [29]. It can be seen that the ionic radii difference (ΔR) between Mn^{2+} ions and Bi^{3+} ion, 0.21 Å, is very similar to the size difference between Mn^{2+} and Ti^{4+}, 0.24 Å. The differences were taken considering the right coordination number for the Bi and the Ti sites. This suggests that the local distortions caused in the first nearest neighbours by the incorporation in the both host site are similar and that can explain the small difference in the solution energies. It is interesting to note that Mn^{2+} incorporation at both host sites is expected to increase the hole defect concentration in the host.

The next defects that should be also considered are ($2Mn_{Bi}' + V_O^{\bullet\bullet}$) and ($Mn_{Ti}'' + V_O^{\bullet\bullet}$) where the Mn^{2+} substitutes at one of the cation sites, and the charge compensation is provided by oxygen vacancies, with solution energy about 5% and 13% higher than the solution energy for the ($Mn_{Bi}' + h^{\bullet}$), respectively. One should not rule out completely this two defect types but if they exist, their concentrations in the matrix are expected to be much lower than the previous ones, especially for the ($Mn_{Ti}'' + V_O^{\bullet\bullet}$).

Table 6 – The solution energies per defect ion for Mn-doped in $Bi_{12}TiO_{20}$ (eV) host.

Mn^{2+}			
Bi site		**Ti site**	
$2Mn_{Bi}' + V_O^{\bullet\bullet}$	4.22	$Mn_{Ti}'' + V_O^{\bullet\bullet}$	4.56
$3Mn_{Bi}' + Bi_i^{\bullet\bullet\bullet}$	8.78	$3Mn_{Ti}'' + 2Bi_i^{\bullet\bullet\bullet}$	13.7
$4Mn_{Bi}' + Ti_i^{\bullet\bullet\bullet\bullet}$	6.52	$2Mn_{Ti}'' + Ti_i^{\bullet\bullet\bullet\bullet}$	9.15
$Mn_{Bi}' + h^{\bullet}$	**4.01**	$Mn_{Ti}'' + 2h^{\bullet}$	4.13
Mn^{3+}		**Mn^{4+}**	
Bi site		**Ti site**	
Mn_{Bi}	3.11	Mn_{Ti}	**-1.58**
Ti site		**Bi site**	
$2Mn_{Ti}' + V_O^{\bullet\bullet}$	1.03	$2Mn_{Bi}^{\bullet} + O_i''$	5.45

$3Mn_{Ti}' + Bi_i^{\bullet\bullet\bullet}$	5.59	$3Mn_{Bi}^{\bullet} + V_{Bi}'''$	5.03
$4Mn_{Ti}' + Ti_i^{\bullet\bullet\bullet\bullet}$	3.33	$4Mn_{Bi}^{\bullet} + V_{Ti}''''$	5.58
$Mn_{Ti}' + h^{\bullet}$	**0.81**	$Mn_{Bi}^{\bullet} + e'$	2.70

For the incorporation of the Mn^{3+} ion, the schemes involving the substitution at Ti^{4+} site compensated by a hole compensation mechanism ($Mn_{Ti}' + h^{\bullet}$) seem to be more energetically favourable compared with substitution at Ti^{4+} site compensated by an oxygen vacancy ($2Mn_{Ti}' + V_O^{\bullet\bullet}$).

The energy difference between these two defects is about 33%, indicating that the first one will probably dominate the dissolution mechanism of Mn^{3+} in the BTO matrix. All the other defect types, including the isovalent substitution of Mn^{3+} at the Bi^{3+} sites, showed much higher formation energies, pointing to the fact that substitutional defects cannot be hypothesized simply considering charge similarities between the substituent and the substituted ions. On the contrary charge difference is just one of the issues and, in some cases as seen here, it is not the most important one. The chemical nature of the species including bonding types, coordination number and ionic radii can be as important as the ionic charges, even in a material with a strong ionic nature.

The dominant defect type induced by the Mn^{3+} doping can be explained in terms of ionic radii difference (ΔR) between the Mn^{3+} doped ion and the possible substituted ions (Bi^{3+} and Ti^{4+}) given in Table 7. In this case, since there is no reported data of Mn^{3+} with coordination number 4, we have taken the data of coordination number 5 as a reasonable approximation [29]. The ionic radii difference (ΔR) for the incorporation at Bi^{3+} (0.38 Å) are approximately two times greater than the incorporation at Ti^{4+} (0.18 Å). The solution energies obtained for the substitution of the Mn^{3+} ion are lower than for the substitution of the Mn^{2+} ion. The results suggest that the Mn^{3+} ion is more stable in the BTO host.

Table 7 – Ionic radii difference between host cations and doped ions.

Doped ions	R_d(CN) (Å)	$\Delta R = \lvert R_h(CN) - R_d(CN) \rvert$	
		$R_{Bi}^{3+}(5)$=0.96 Å	$R_{Ti}^{4+}(4)$=0.42 Å
Mn^{2+}	0.66 (4)		0.24
	0.75 (5)	0.21	
Mn^{3+}	-		
	0.58 (5)	0.38	
Mn^{4+}	0.39 (4)		0.03
	-		

CN stands for coordination number, R_h(CN) and R_d(CN) indicate the radii of host and doped cations, respectively. The values of the effective ionic radii are from Ref. [29].

The incorporation of Mn^{4+} ions shows the same tendency observed for the Mn^{3+} ions, i.e., it prefers to incorporate at Ti^{4+} site, as can be confirmed by the

negative solution energies (-1.58 eV). On the other hand, the incorporation at Bi^{3+} site is highly unfavourable, with solution energies that vary from 2 to 5 eV. The calculated ionic radii difference (ΔR) between the Mn^{4+} doped ion and the Ti^{4+} ion is a small value, 0.03 Å. The results mean that little distortions are caused by substitution of Ti^{4+} by Mn^{4+} and, consequently, a small energy is required for its replacement. It can be noticed that Mn ions in the valence state 4+ have lower solution energies than Mn in valence 2+ and 3+. This shows that Mn^{4+} is more stable in the BTO host.

Figure 3a presents the XANES spectra at Mn K edge. The data were analysed from direct comparison with reference materials MnO, Mn_2O_3, and MnO_2, in which Mn ions assume oxidation numbers Mn^{2+}, Mn^{3+} and Mn^{4+}. The absorption edge shifts towards higher values as the valence increases. This effects is due partly by an increasing attraction between the nucleus and 1s core electrons and partly by the effect of final-state wave functions. The spectral region just below *K*-edge XANES monitors the electronic transitions from 1*s* core level to unoccupied *p* or *d* states of the absorbing atom. In Fig. 2a it can be observed a pre-edge peak for BTO: Mn and also for all the references measured. The position of this peak is valence-dependent and also shifts positively with valence states. Its intensity, however, is symmetry-dependent, and decreases with increasing coordination number [30]. Figure 3b presents the linear relationships of both energies of the pre-edge peak and absorption edge as a function of the oxidation number of Mn. For BTO: Mn, pre-edge peak position is E = 6541eV whereas the edge position is E = 6549 eV. In both cases, these values are between the ones observed for the references Mn^{3+} and Mn^{4+}, which is consistent with mixed valence 3+ and 4+ of the absorber element. According to Table 6, the defects with lowest energy cost for Mn^{3+} and Mn^{4+} are, respectively, $Mn_{Ti}' + h^{\bullet}$ and Mn_{Ti}. In both cases, Mn ions would occupy Ti sites. This information was further investigated in this work through EXAFS analysis.

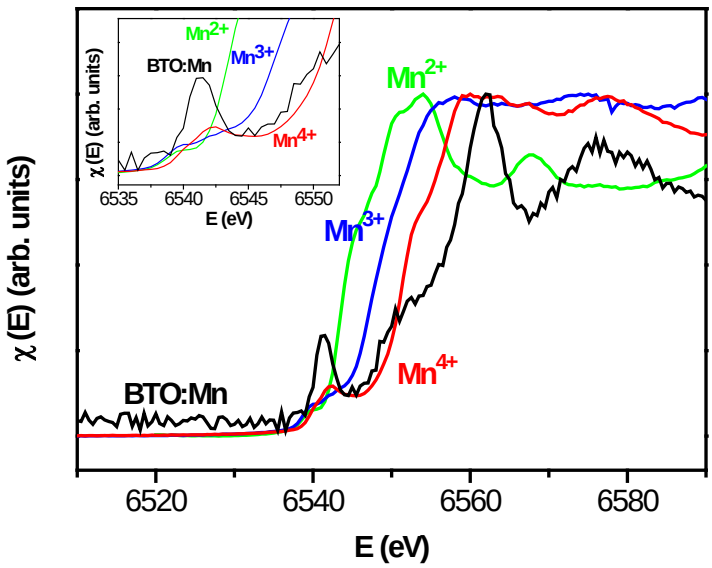

(a)

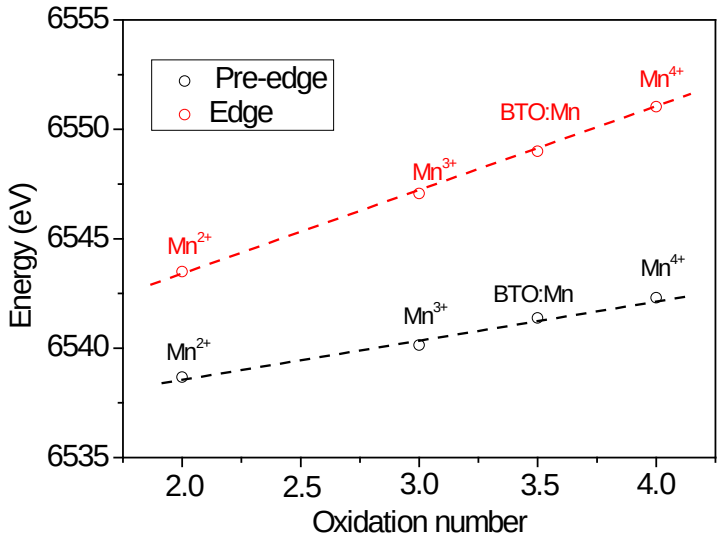

(b)

Figure 3 – (a) XANES spectra of BTO: Mn measured in fluorescence mode of the Mn K-edge; (b) Pre-edge and edge energies position versus Mn valence. Values evaluated for BTO: Mn indicate mixed valence 3+ and 4+ for the absorber element.

EXAFS measurements were used to probe the local environment of Mn dopant in the BTO structure. Experimental data were processed using ATHENA software [31]. A Normalized χ(k) signal was weighted by k^2 and Fourier transformed to R space, giving the radial distribution function presented in Fig. 3. After this pre-treatment, two radial distributions were tentatively fitted to experimental data, supposing Mn either in Bi^{3+} or Ti^{4+} sites. This procedure employed the software ARTEMIS [31] and the crystallographic data of ref. [26]. The fitting parameters were radial distance (R) and mean square displacement (σ^2), also known as Debye-Waller factor. The calculated FT curves obtained in each case are also presented in Fig. 3. Small oscillations below 1 Å are measurement artefacts and the first intense peak is due to the nearest oxygen neighbours. High attenuation of photoelectrons by heavy Bi atoms, as well as low concentration of Mn in the crystalline host, precludes the analysis of more distant coordination shells. Therefore, we will restrict the EXAFS analysis to the comparison between experimental and calculated position of the nearest oxygens, departing from structural models with either Mn_{Bi} or Mn_{Ti} defects. A visual analysis of the curves indicates that the fitting of Fig. 3b is more realistic. The atomic distances between Mn and the first coordination shell obtained from the fittings were R = 2.2±0.3 with σ^2 = 0.02±0.01 for Mn_{Bi}, and R = 1.707±0.005 with σ^2 = 0.001±0.003 for Mn_{Ti}. The smaller values obtained for σ^2 and for the standard deviation of R found using Mn_{Ti} model indicate that this model is the most suitable, according to the EXAFS experiments. This result corroborates the lowest solution energy determined for the defects involving substitutional Mn in Ti site (see Table 6).

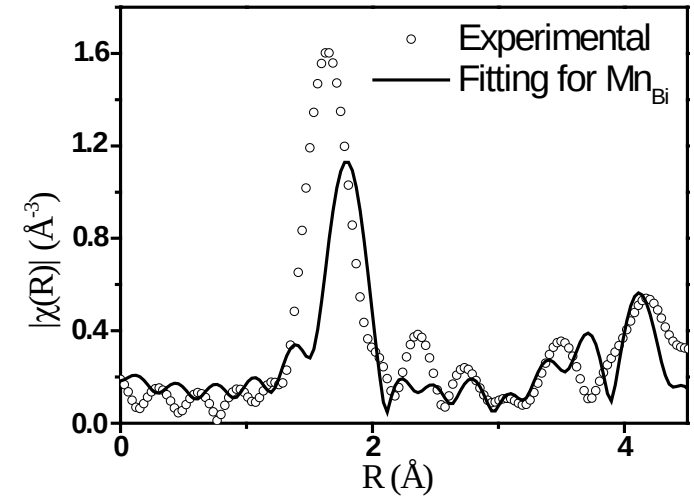

(a)

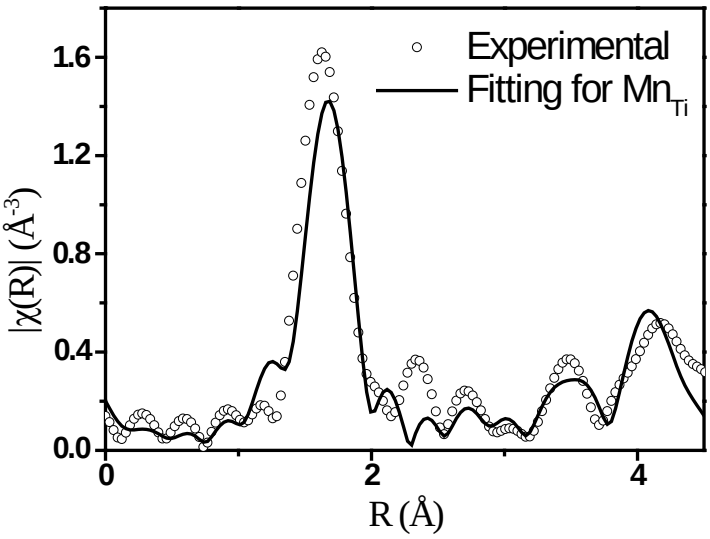

(b)

Figure 4 – Fourier transforms of EXAFS experimental data (open circles), measured near Mn K edge, and simulation (solid line) supposing (a) Mn_{Bi} or (b) Mn_{Ti} substitutional defects.

Figure 5 presents dark AC conductivity of pure and Mn-doped BTO, measured isothermally at temperatures between 225 and 400 ^{o}C and f = 10 kHz. The experimental error bars are smaller than the symbol size. It can be noticed that BTO: Mn is more conductive than the pure sample for all temperatures tested, and that at higher temperatures this effect is more evident. It was reported in the literature that dark conductivity in BTO host is *p*-type, associated to antisite defect with charge compensation by trapped holes (Bi'_{Ti}+$h^{\bullet}$)[7]. This defect is considered the acceptor centre responsible for electrical dark conduction [11]. Considering atomistic modelling and XAS results of the present work, additional defects (Mn'_{Ti}+$h^{\bullet}$) and Mn_{Ti}^{x} will be present in the Mn-doped sample. These results are consistent with a higher

concentration of p-type charge carriers in doped samples, leading to a higher AC dark conductivity.

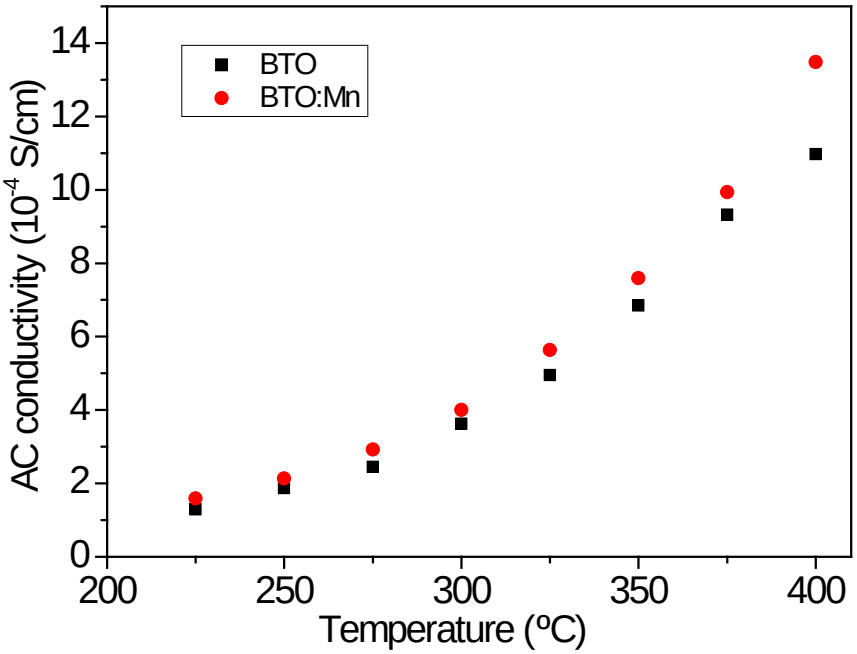

Figure 5 – AC conductivity of pure and Mn-doped BTO.

4. Conclusions

Pure and Mn-doped $Bi_{12}TiO_{20}$ samples were obtained by solid-state reaction and studied by the experimental techniques XAS, XRD and AC conductivity, combined with atomistic simulation, in order to determine the oxidation number and site occupancy of Mn in BTO matrix. A good agreement between experimental and simulation results was achieved, indicating two different possible extrinsic defects induced by Mn-doping. XANES results point to a mixed 3+ and 4+ valence of Mn, which would occupy Ti^{4+} site in both cases. Charge compensation by holes is the most energetically favourable process and is responsible by the enhancement observed for the AC dark conductivity, which is due to p-type charge carriers.

Acknowledgements

The authors wish to acknowledge Brazilian Synchrotron Light Laboratory (LNLS), CAPES, CNPq, FAPITEC/SE and FINEP for the financial support.

References

[1] R. Chen, W. Hu, L. Zou, W. Xie, D. Bao, Ceram. Int. 41 (2015) S829.

[2] X. Zhu, J. Zhang, F. Chen, Appl. Catal. B Environ. 102 (2011) 316.

[3] H. Xu, Y. Zhang, H. Zhang, H. Yu, Z. Pan, Y. Wang, S. Sun, J. Wang, R.I. Boughton, Opt. Commun. 285 (2012) 3961.

[4] A. Veber, Š. Kunej, R. Cerc Korošec, D. Suvorov, J. Eur. Ceram. Soc. 30 (2010) 2475.

[5] S.V. Nistor, M. Stefan, E. Goovaerts, F. Ramaz, B. Briat, J. Magn. Reson. 259 (2015) 87.

[6] A.E. Nogueira, E. Longo, E.R. Leite, E.R. Camargo, Ceram. Int. 41 (2015) 12073.

[7] J.F. Carvalho, R.W.A. Franco, C.J. Magon, L.A.O. Nunes, F. Pellegrini, A.C. Hernandes, Mater. Res. 2 (1999).

[8] J.F. Carvalho, R.W.. Franco, C.. Magon, L.A.. Nunes, A.. Hernandes, Opt. Mater. (Amst). 13 (1999) 333.

[9] V. Marinova, K.Y. Hsu, S.H. Lin, R.C. Liu, Y.H. Lin, in:, M. Hrabovský, J.T. Sheridan, A. Fimia-Gil (Eds.), 2013, p. 877605.

[10] J. Frejlich, R. Montenegro, T.O. dos Santos, J.F. Carvalho, J. Opt. A Pure Appl. Opt. 10 (2008) 104005.

[11] R. Montenegro, A. Shumelyuk, R. Kumamoto, J.F. Carvalho, R.C. Santana, J. Frejlich, Appl. Phys. B 95 (2009) 475.

[12] M.F.C. Gurgel, J.W.M. Espinosa, A.B. Campos, I.L.V. Rosa, M.R. Joya, A.G. Souza, M.A. Zaghete, P.S. Pizani, E.R. Leite, J.A. Varela, E. Longo, J. Lumin. 126 (2007) 771.

[13] J.Y. Son, Y.-S. Shin, Thin Solid Films 520 (2012) 3017.

[14] A.V. Egorysheva, V.I. Burkov, Y.F. Kargin, A.Y. Vasil'ev, V. V. Volkov, V.M. Skorikov, Inorg. Mater. 37 (2001) 817.

[15] A.L. Ankudinov, B. Ravel, J.J. Rehr, S.D. Conradson, Phys. Rev. B 58 (1998) 7565.

[16] R.A. Jackson, J.A. Dawson, M.E.G. Valerio, Z.S. Macedo, Opt. Mater. 32 (2010) 1375.

[17] C. Pirovano, Solid State Ionics 140 (2001) 115.

[18] M.E.G. Valerio, R.A. Jackson, Z.S. Macedo, Phys. Status Solidi 2 (2005) 485.

[19] L. Bleicher, J.M. Sasaki, C.O. Paiva Santos, J. Appl. Crystallogr. 33 (2000) 1189.

[20] D.J. Santos, L.B. Barbosa, R.S. Silva, Z.S. Macedo, Adv. Condens. Matter Phys. 2013 (2013) 1.

[21] B. Dick, A. Overhauser, Phys. Rev. 112 (1958) 90.

[22] J.D. Gale, J. Chem. Soc. Faraday Trans. 93 (1997) 629.

[23] G.V. Lewis, C.R.. Catlow, J. Phys. Chem. Solids 47 (1986) 89.

[24] G.V. Lewis, C.R.A. Catlow, J. Phys. C Solid State Phys. 18 (1985) 1149.

[25] N.F. Mott, M.J. Littleton, Trans. Faraday Soc. 34 (1938) 485.

[26] D.C.N. Swindells, J.L. Gonzalez, Acta Crystallogr. Sect. B Struct. Sci. 44 (1988) 12.

[27] CRC Press, ed., Handbook of Chemistry and Physics, 65th ed, CRC Press, Boca Raton, 1985.

[28] Handbook of Chemistry and Physics, 65th ed., CRC Press, Boca Raton, FL, 1985.

[29] R.D. Shannon, Acta Crystallogr. Sect. A 32 (1976) 751.

[30] T. Yamamoto, X-Ray Spectrom. 37 (2008) 572.

[31] B. Ravel, M. Newville, J. Synchrotron Radiat. 12 (2005) 537.